Large Eddy Simulation of Jets Laden with Evaporating Drops

Anthony Leboissetier*, Nora Okong'o† and Josette Bellan‡
Jet Propulsion Laboratory
California Institute of Technology
Pasadena CA 91109-8099

LES of a circular jet laden with evaporating liquid drops are conducted to assess computational-drop modeling and three different SGS-flux models: the Scale Similarity model (SSC), using a constant coefficient calibrated on a temporal mixing layer DNS database, and dynamic-coefficient Gradient and Smagorinsky models (GRD and SMD, respectively). The GRD model was used for LES of an unforced jet, that compared well to previous DNS at the same jet-diameter Reynolds number of 500. For a forced jet at the same Reynolds number, where the inlet streamwise velocity was perturbed, the three SGS models were compared. The LES had similar results in representing the time-evolution of globally-averaged vorticity and enstrophy, and of ensemble-averaged drop temperature and size. When compared at the same physical time, the LES has similar spatial distributions of vorticity, drop number density and vapor mass fraction. The jet displayed a series of vortices induced by the forcing, but lacked small scale structures, for which the SMD model has previously shown to perform poorly in LES of a temporal mixing layer. Using the GRD model, the number of computational drops (each representing a number of physical drops) was reduced from the number of physical drops by up to a factor of 64; however, a reduction factor of 32 was found to be the maximum that yielded numbers and spatial distributions of physical drops similar to those obtained at lower reduction factors.

1 Introduction

Two-phase (TP) flows occur in many important natural and industrial processes. In many of these processes, such as household cleaning products, pharmaceutical inhalers, office printers, gas turbine engines and spray-chemical-conversion reactors, the gaseous carrier phase transports particles of a liquid dispersed phase, and the two phases exchange mass, momentum and energy. Direct Numerical Simulation (DNS) of TP flows is a useful research tool to investigate the interaction between the carrier phase and the dispersed (particulate) phase. Recent TP DNS include those for solid particles without phase change in isotropic turbulence,[1,2] and those for evaporating drops in isotropic turbulence,[3,4] temporal mixing layers[5–7] and jets.[8] In these DNS, the gas-phase was computed in an Eulerian frame and the drops were individually tracked in a Lagrangian frame. Following Boivin et al.,[1] the terminology 'DNS' is retained to refer to simulations in which the turbulent scales of the gas phase are resolved, the particles are smaller than the Kolmogorov scale and the interaction between the gas phase and the particles is modeled. However, DNS of turbulent flows are still relatively computationally expensive.

The intent of Large Eddy Simulation (LES) is to replicate the results of the DNS while reducing both the number of grid points and the number of computed drops. This reduction can be attained by calculating only the largest scales of the turbulence while modeling the subgrid scales (SGSs), and by using computational drops to represent the physical drops, thereby reducing the computational demands of DNS. However, LES has additional modeling requirements compared to DNS. The gas-phase LES equations are derived by spatially filtering the DNS gas-phase equations, and contain terms that need to be modeled: the SGS fluxes arising from filtering the convective terms, and the filtered source terms (FSTs) representing the effects of the drops on the filtered LES field. Recent LES of TP flows have considered an incompressible gas phase laden with small solid particles, with one-way[9–14] or two-way[9,14] coupling, and used physical or computational particles whose evolution was entirely governed by the resolved flow field, that is, neglecting SGS effects on drop evolution. Because the SGS modeling requirement in these LES was confined to the gas phase, SGS-flux models for incompressible single-phase (SP) flow could be used; these LES used Smagorinsky[15] (SM) SGS-flux modeling, in constant- or dynamic-coefficient implementations (denoted SMC or SMD). The SM model is based on eddy viscosity concepts, and assumes the SGS fluxes to be proportional to the strain rate. The SMC model shows poor correlations with the SGS quantities,[7] but has been

*Post-Doctoral Scholar, AIAA Member.
†Scientist, AIAA Senior Member.
‡Senior Research Scientist, AIAA Associate Fellow (corresponding author, josette.bellan@jpl.nasa.gov).

used in recent TP LES of reacting jets.[16,17] Although dynamic modeling, wherein the model coefficients are computed from the LES during the LES, is considered more accurate, its increased computational costs discourage its use in engineering problems, and the SMC model is still preferred to the SMD model in many applications. Other approaches designed to increase the accuracy of LES modeling, applied to LES of jets, include unstructured mesh algorithms[18] and grid-averaged Lagrangian drop-modeling.[19] The problem of robust and accurate, as well as computationally efficient, TP LES models therefore remains an active research area.

LES models for TP flows with evaporating drops have been developed by Okong'o and Bellan[7] using a DNS database of a temporal mixing undergoing transition to turbulence, and then validated in LES of the same flow.[20] The LES were performed with constant-coefficient SGS-flux models, using coefficients calibrated on the DNS database, and with dynamic-coefficient SGS-flux models. The three SGS models that were consistently numerically stable were the constant-coefficient Scale Similarity[21] model (SSC) and the dynamic Gradient (GRD) and SMD models, the SMD model being combined with the Yoshizawa[23] model for trace of the SGS momentum fluxes. The Gradient[24] model is based on a Taylor series expansion of the SGS fluxes, while the SSC model attempts to deduce the SGS behavior from that of the smallest resolved scales, and forms the premise of dynamic modeling.[25–27] All LES used a grid spacing four times that of the DNS, resulting in a 64-fold reduction in the number of grid points. The computational drop model involved representing N_R physical drops by one computational drop, and tracking the computational drops using the same evolution equations as the physical drops, but having the drops encounter the filtered LES field instead of the DNS field, that is, neglecting direct SGS effects on drop evolution. The SMD model was found to be unable to achieve transition to turbulence, attributed to its overly dissipative nature, while the SSC and GRD models performed well in replicating the DNS field for both single-phase (SP) and TP flows. The GRD and SSC models had good predictions of the spatial distribution of the drop number density and of the vapor mass fraction, while the SMD model did not. It was found that the computational-drop model retained accuracy as N_R was increased, up to a value of 32.

The LES mixing layer study[20] concluded that the developed LES models[7] needed to be further tested in a spatial configuration, with the intent of eventual validation with experimental data. To this end, LES of a jet laden with evaporating liquid drops have been conducted, and are compared with DNS performed for similar flow conditions.[8] Section 2 of this paper presents the highlights of the LES methodology, the LES models and the flow configuration. Section 3 discusses the jet LES results, including flow visualizations, and finally conclusions and areas for future work are summarized in the last section.

2 LES Methodology

The LES methodology is described by Okong'o and Bellan,[7] along with details of the underlying DNS methodology which is based on the formulation of Miller and Bellan.[5] The governing equations are formulated in an Eulerian frame for the gas phase and in a Lagrangian frame for the drops. The gas phase consists of two species: the carrier gas and the vapor evolving from the drops. The drops are treated as point sources of mass, momentum and energy. This assumption is justified by the dilute (i.e. volumetrically small, $O(10^{-3})$) loading and the size of each particle being much smaller than the Kolmogorov scale.[1]

2.1 Gas-Phase Equations

The vector of gas-phase conservative variables is defined as $\phi = \{\rho,\ \rho u_i,\ \rho e_t,\ \rho Y_V\}$ where ρ is the density, u_i is the velocity in the x_i coordinate direction, e_t is the total energy (internal energy, e, plus kinetic energy, $u_i u_i/2$) and Y_V is the vapor (subscript V) mass fraction (the carrier gas, subscript C, mass fraction is Y_C; $Y_C + Y_V = 1$). The gas-phase LES equations are obtained from spatial filtering of the DNS equations; for a variable ψ, $\bar{\psi}$ denotes spatial filtering whereas $\tilde{\psi} = \overline{\rho\psi}/\bar{\rho}$ denotes Favre (density-weighted) spatial filtering. The filtered flow field is denoted as $\bar{\phi}$, and $\bar{\Delta}$ is the filter width for the present LES which use a cubic-top hat filter. The adopted form of the gas-phase LES equations is:[7]

$$\frac{\partial \bar{\rho}}{\partial t} + \frac{\partial \left(\bar{\rho}\tilde{u}_j\right)}{\partial x_j} = \bar{S}_I \tag{1}$$

$$\frac{\partial \left(\bar{\rho}\tilde{u}_i\right)}{\partial t} + \frac{\partial \left(\bar{\rho}\tilde{u}_i\tilde{u}_j\right)}{\partial x_j} = -\frac{\partial \left[p\left(\bar{\phi}\right)\right]}{\partial x_i} + \frac{\partial \sigma_{ij}\left(\bar{\phi}\right)}{\partial x_j} + \bar{S}_{II,i} - \frac{\partial \left(\bar{\rho}\tau_{ij}\right)}{\partial x_j} \tag{2}$$

$$\frac{\partial \left(\bar{\rho}\tilde{e}_t\right)}{\partial t} + \frac{\partial \left(\bar{\rho}\tilde{e}_t\tilde{u}_j\right)}{\partial x_j} = -\frac{\partial \left[p\left(\bar{\phi}\right)\tilde{u}_j\right]}{\partial x_j} - \frac{\partial q_j\left(\bar{\phi}\right)}{\partial x_j} + \frac{\partial \left[\sigma_{ij}\left(\bar{\phi}\right)\tilde{u}_i\right]}{\partial x_j} + \bar{S}_{III} - \frac{\partial \bar{\rho}\zeta_j}{\partial x_j} - \frac{\partial}{\partial x_j}\left[\bar{\rho}\tau_{ij}\tilde{u}_i\right] \tag{3}$$

$$\frac{\partial(\bar{\rho}\tilde{Y}_V)}{\partial t} + \frac{\partial(\bar{\rho}\tilde{Y}_V\tilde{u}_j)}{\partial x_j} = -\frac{\partial j_{Vj}\left(\bar{\phi}\right)}{\partial x_j} + \bar{S}_I - \frac{\partial \left(\bar{\rho}\eta_j\right)}{\partial x_j} \tag{4}$$

where the SGS fluxes are

$$\tau_{ij} = \widetilde{u_i u_j} - \tilde{u}_i\tilde{u}_j,\ \zeta_j = \widetilde{hu_j} - \tilde{h}\tilde{u}_j,$$
$$\eta_j = \widetilde{Y_V u_j} - \tilde{Y}_V\tilde{u}_j, \tag{5}$$

and the FSTs are $\bar{S} = \{\bar{S}_I, \bar{S}_{II,i}, \bar{S}_{III}, \bar{S}_I\}$. The pressure ($p$), the enthalpy ($h$), the viscous stresses (σ_{ij}), the heat flux (q_j) and the vapor mass flux (j_{Vj}) have the same form as for DNS:

$$p(\phi) = \rho R(\phi) T(\phi), \tag{6}$$

$$h(\phi) = C_p(\phi) T(\phi) + h_V^0 Y_V = h_C Y_C + h_V Y_V, \tag{7}$$

$$e(\phi) = C_v(\phi) T(\phi) + h_V^0 Y_V = e_C Y_C + e_V Y_V, \tag{8}$$

$$\sigma_{ij}(\phi) = 2\mu \left(S_{ij} - \frac{1}{3} S_{kk} \delta_{ij} \right), \tag{9}$$

$$j_{Vj}(\phi) = -\rho D \frac{\partial Y_V}{\partial x_j} - \rho D \left(\frac{Y_V}{m_V} + \frac{Y_C}{m_C} \right) (m_C - m_V) \frac{Y_V Y_C}{p(\phi)} \frac{\partial p(\phi)}{\partial x_j} \tag{10}$$

$$q_j(\phi) = -\lambda \frac{\partial [T(\phi)]}{\partial x_j} + [h_V(\phi) - h_C(\phi)] j_{Vj}(\phi), \tag{11}$$

assuming a calorically perfect gas where $R(\phi) = Y_V R_V + Y_C R_C$, $R_V = R_u/m_V$, $R_C = R_u/m_C$, R_u is the universal gas constant and m_C and m_V are the molar weights of the carrier gas and vapor respectively. The mixture heat capacity at constant pressure is $C_p(\phi) = C_{p,V} Y_V + C_{p,C} Y_C$, where $C_{p,C}$ and $C_{p,V}$ are assumed constant, and h_V^0 is the reference vapor enthalpy at (T^0, p^0) which accounts for the enthalpy difference between the vapor and carrier gas at the reference conditions. The temperature (T) is computed from e, where C_v is the mixture heat capacity at constant temperature ($C_v = C_p - R$);

$$S_{ij}(\phi) = \frac{1}{2} \left(\frac{\partial u_i}{\partial x_j} + \frac{\partial u_j}{\partial x_i} \right) \tag{12}$$

is the rate of strain. The viscosity (μ), the diffusion coefficient (D), and the thermal conductivity (λ) are assumed constant, and will be defined through the Prandtl and Schmidt numbers, $\mathrm{Pr} = \mu C_p/\lambda$ and $Sc = \mu/(\rho D)$.

2.2 Liquid-Phase Equations

The LES uses N_{cd} computational drops to represent the N_d physical drops, that is each computational drop represents $N_R \equiv N_d/N_{cd}$ physical drops. The LES computational drops, denoted $\bar{Z}$, follow the DNS evolution equations[5] for physical drops Z:

$$dZ/dt = \Sigma(\psi_f, \psi_s, Z), \quad d\bar{Z}/dt = \Sigma(\tilde{\psi}_f, \tilde{\psi}_s, \bar{Z}), \tag{13}$$

where Σ has the same functional form for LES as in the DNS but is based on $\tilde{\psi}$ and $\bar{Z}$ instead of ψ and Z. We define $Z = \{X_i, v_i, T_d, m_d\}$ as the physical drop field with position X_i, velocity v_i, temperature T_d, and mass m_d;

$$\Sigma = \left\{ v_i, \frac{F_i}{m_d}, \frac{Q + \dot{m}_d L_V(Z)}{m_d C_L}, \dot{m}_d \right\}, \tag{14}$$

where F_i is the drag force, Q is the heat flux, $\dot{m}_d$ is the evaporation rate, and C_L is the heat capacity of the drop liquid. L_V is the latent heat of vaporization, which here is a linear function of temperature, $L_V = h_V^0 - (C_L - C_{p,V})\hat{T}_d$. The drop evolution depends on the gas-phase primitive variables, $\psi(\phi) = \{u_i, T, Y_V, p\}$, evaluated either at the drop surface (subscript s) or at the drop far-field (subscript f). The far-field variables are taken as the gas-phase primitive variables interpolated to the drop locations. The detailed expressions[5] for F_i, Q, and $\dot{m}_d$ involve validated correlations for point drops which are based on Stokes drag, with the particle time constant defined as[22] $\tau_d = \rho_L d^2/(18\mu)$, where ρ_L is the density of the liquid and d is the drop diameter (spherical drops; $m_d = \rho_L \pi d^3/6$):

$$F_i(\psi_f, Z) = \frac{m_d}{\tau_d} f_1 (u_{i,f} - v_i) \tag{15}$$

$$Q(\psi_f, Z) = \frac{m_d}{\tau_d} \frac{Nu}{3\,\mathrm{Pr}} C_{p,f} f_2 (T_f - T_d) \tag{16}$$

$$\dot{m}_d(\psi_f, \psi_s, Z) = -\frac{m_d}{\tau_d} \frac{Sh}{3Sc} \ln(1 + B_M) \tag{17}$$

Here, f_1 is an empirical correlation to correct the Stokes drag for finite drop Reynolds numbers and the mass transfer number is $B_M = (Y_{V,s} - Y_{V,f})/(1 - Y_{V,s})$. The Nusselt, Nu, and Sherwood, Sh, numbers are empirically modified for convective corrections to heat and mass transfer based on the Ranz-Marshall correlations. Except for τ_d, which depends on μ, Eqs. 15–17 depend essentially on ratios of transport properties through non-dimensional numbers. Therefore, the value of τ_d and thus for a given liquid and drop size, the value of μ determines the interaction time between drops and gas.

2.3 LES Models

The gas-phase LES equations (Eqs. 1–4) contain terms that cannot be computed directly from the filtered flow field $\bar{\phi}$ and that need to be modeled, namely, (1) the SGS fluxes (τ_{ij}, ζ_j, η_j) and (2) the FSTs.

2.3.1 Subgrid-scale flux models

For the SGS fluxes, we consider the three models previously used for LES of a temporal mixing layer:[20] SSC, using a second, test-level, filter of width $\hat{\Delta} = \bar{\Delta}$ and the DNS-calibrated[7] constant $C_{SS} = 1.996$, and SMD and GRD using $\hat{\Delta} = 2\bar{\Delta}$. Here, the GRD and SMD models use different coefficients for each type of SGS flux, one for τ_{ij}, one for ζ_j and one for η_j, denoted C_τ, C_ζ and C_η respectively; these coefficients are spatially constant in the domain. SGS-flux models were found to be absolutely necessary in order to compute flows on the LES grids as the simulations performed with no SGS model crashed, this being evidence that the high accuracy of the numerical method (see Section 2.5) does not allow under-resolved computations.

2.3.2 Models for filtered source terms

The exact FSTs for the top-hat filter used in the present LES are

$$\bar{S} = (1/V_f) \sum_{\alpha=1}^{N_\alpha} \left[S_d \left(\psi_f, \psi_s, Z \right) \right]_\alpha , \qquad (18)$$

a volume-average over the N_α physical drops within the filtering volume V_f. The individual physical-drop source contributions $S_d(\psi_f, \psi_s, Z) = \{S_{I,d}, S_{II,i,d}, S_{III,d}, S_{I,d}\}$, are

$$\begin{aligned} S_{I,d} &= -\dot{m}_d, \; S_{II,i,d} = -\left[F_i + \dot{m}_d v_i \right], \\ S_{III,d} &= -\left[F_i v_i + Q + \dot{m}_d \left(v_i v_i / 2 + h_{V,s} \right) \right]. \end{aligned} \qquad (19)$$

The FSTs are modeled from the computational drop field, $\tilde{Z}$, and the filtered primitive variables $\tilde{\psi}$:

$$\bar{S}\left(\tilde{\psi}, \tilde{Z} \right) = (N_R/V_f) \sum_{\beta=1}^{N_\beta} \left[S_d \left(\tilde{\psi}_f, \tilde{\psi}_s, \tilde{Z} \right) \right]_\beta \qquad (20)$$

where the summation is over the N_β computational drops within the filtering volume V_f.

2.4 Flow configuration

The initial configuration of the simulation, similar to the geometry of Abdel-Hameed and Bellan,[8] is illustrated in Fig. 1 where the streamwise (x_1), the cross-stream (x_2), and the spanwise (x_3), coordinates are shown, and the domain lengths are L_1, L_2 and L_3 in each direction. For all the simulations performed herein, D_J=0.02m is the diameter of the jet circular orifice, centered at $(x_2, x_3) = (0, 0)$ in the inlet ($x_1 = 0$) plane. Initially, the domain of simulation is devoid of drops; during the simulation these are injected through the orifice. Navier-Stokes Characteristic Boundary Conditions (NSCBC)[28] are used: an inlet condition at $x_1 = 0$ and outlet boundary conditions on the other boundaries.

The free-stream velocity ($U_0 = M_{c,0} a_{C,0}$) is calculated from a specified value of the convective Mach number ($M_{c,0}$) based on the carrier gas initial speed of sound ($a_{C,0} = \sqrt{R_C T_{C,0} C_{p,C} / C_{v,C}}$ where $T_{C,0}$ is the initial uniform temperature of the carrier gas at the initial uniform pressure); the carrier gas is the sole initial species in the gas phase. The jet exit speed (U_J) is determined from the exit Mach number (M_J). The inflow profile is smoothed by a tanh function of width $\delta_J = D_J/25$ and, to promote the development of coherent structures, is forced using sinusoidal perturbations of amplitude $A_i = A_0/2^i$ and frequency $f_i = 2^i f_0$ (for $i = 0, \ldots, 4$), related to the Strouhal number as $f_0 = StrU_J/D_J$; the values used are $A_0 = 0.2$ and $Str = 0.2$. The specified value of the initial Reynolds number, $\mathrm{Re}_0 = \rho_0 \Delta U_0 D_J / \mu$, where ρ_0 is the initial gas density, is used to calculate μ. All thermo-physical properties are for air as the carrier gas and decane as the drop liquid[6] (ρ_L =642 kg/m^3) with Pr = Sc=0.697.

The LES were performed for the same conditions as the DNS:[8] $\mathrm{Re}_0 = 500$, $M_{c,0}$=0.05, M_J=0.35, $T_{C,0}$=350K, ρ_0=0.9415kg/m^3, ΔU_0=112.3m/s (with $U_J = 131$m/s and $U_0 = 18.7$m/s). The drops have initial diameter $d_0 = 50$ μm, temperature $T_{d,0}$=325K and velocity $V_1 = 0.75 U_J$. The number of drops injected at each time step is determined by the injected liquid flux $\dot{m}_L = 0.012$ kg/s. The initial drop size based on the Stokes number $St = \tau_d \Delta U_0 / \delta_J$ is St =2.79, close to the initial Stokes number of 3 of the temporal mixing layer DNS and LES.[5,7,20] Drops are removed from the simulation once they diminish below 10% of their initial mass, in contrast to DNS where drops reaching the minimum size were 'frozen' but not removed from the computational domain. Also, the DNS inflow had $Y_V = 0.03$ at the orifice, while the LES has no vapor in the inflow, so the LES flow is allowed to completely determine Y_V.

2.5 Numerical procedure

The LES used the same numerical scheme as the DNS.[8] The LES equations were numerically solved using a fourth-order explicit Runge-Kutta temporal integration for time derivatives and an implicit sixth-order central finite differences with eighth-order filtering for spatial derivatives.[29] A fourth-order Lagrange interpolation procedure was used to obtain gas-phase variable values at the drop locations.[5] The eighth-order filtered was applied every four time steps, and the dynamic coefficients were updated at the same interval.

3 Results

3.1 Unforced Jet

For comparison with the DNS of circular unforced jets, LES were first performed using the GRD model with $N_R = 1$, without any forcing (A_0=0). The domain size was $L_1 = 2L_2 = 2L_3 = 8D_J$=0.16m. The DNS used 240×180×180 grid points, whereas the LES used 128×64×64 points. The main determinant of the LES resolution was the representation of the circular orifice, although TP DNS[8] showed little influence of the orifice geometry for circular, square and triangular orifices having the same equivalent jet diameter. Both DNS and LES reached steady state by $t^* = 14$. In the DNS,[8] the criterion for the achievement of the jet steady-state was the invariance in time of the mass flux difference $(Q - Q_0)/Q_0$, where $Q(x_1) = \iint \rho u_1 dx_2 dx_3$ is the streamwise mass flux and $Q_0 = Q(0)$. This criterion has previously been applied to SP unforced jets.[30] Figure 2 represents the mass flux at $t^* = 14$ for GRD LES, which is seen to be similar to that from the DNS[8] at $t^* = 14.2$, also plotted. The LES mass flux agrees well with the DNS near the inlet, but exceeds it downstream, indicating an overprediction of entrainment. For forced jets, Q_0 varies in time, and $(Q - Q_0)/Q_0$ will not reach a steady state. Therefore, an alternative criterion for the steady state of

unforced jets, that will also be applicable for determining the stationary state of forced jets, is when N_d (the number of physical drops in the domain) becomes constant. Using this criterion, the LES reaches steady state at $t^* = 14$, with $N_d = 484\,000$.

The LES is compared to the DNS results[8] for the vorticity,

$$\omega_1 = \frac{\partial u_3}{\partial x_2} - \frac{\partial u_2}{\partial x_3},\ \omega_2 = \frac{\partial u_1}{\partial x_3} - \frac{\partial u_3}{\partial x_1},\ \omega_3 = \frac{\partial u_2}{\partial x_1} - \frac{\partial u_1}{\partial x_2}, \tag{21}$$

enstrophy ($\omega_i\omega_i$), drop number density (ρ_n) and vapor mass fraction (Y_V). For LES, $\rho_n = N_R N_\beta / V_f$, where N_β is the number of computational drops in the filtering volume V_f, whereas for DNS, $\rho_n = \sum_{\alpha=1}^{N_\alpha} (w_\alpha / V)$, a weighted sum over the N_α physical drops, proportional to the drop distance, in the computational volume V. For convenience, the tilde and overbar denoting filtered quantities are omitted; DNS refers to unfiltered quantities, whereas LES refers to filtered quantities. The steady state ω_3, $\omega_i\omega_i$, ρ_n and Y_V are depicted in Figs. 3 and 4 at the center-plane ($x_3 = 0$), while Figs. 5 and 6 show ω_3 and ρ_n, respectively, at the same time at three different downstream locations (x_1/D_J=2.5, 5.0 and 7.5). The LES closely matches the steady state distributions of the DNS results, as seen in the contour plots in Figs. 3–6. Some discrepancies are observed in ρ_n and Y_V, as the DNS inflow has $Y_{V_J} = 0.03$ at the jet, while the LES has no vapor in the inflow; furthermore, for the DNS, drops reaching the minimum size were 'frozen' but not removed from the computational domain. The presence of vapor retards evaporation, leading to fewer evaporated drops and hence a higher ρ_n (Figs. 4 and 6). However, the jet is not saturated, so Y_V continues to increase downstream, resulting in an overall higher Y_V for the DNS than the LES (Fig. 4). These discrepancies have little impact on the jet dynamics, as the vorticity levels are comparable in the DNS and the LES (Figs. 3 and 5).

3.2 Forced Jet

For the forced jet, LES were performed using the SMD, GRD and SSC SGS-flux models. These simulations, summarized in Table 1, were performed for all models using $N_R = 1$, and additionally for the GRD model using N_R values of 8, 16, 32 and 64. The domain was slightly smaller than for the unforced jet: $L_1 = 3L_2 = 3L_3 = 9D_J$=0.18m with 144×48×48 grid points. Since the jet is forced, it does not reach a steady-state, so the simulations were continued until a stationary state, that is, when the time-averaged statistics are invariant over each cycle of the forcing. Indicated in Table 1 are $N_d(=N_R N_{cd})$ and $N_{d,evap}$ (the cumulative number of drops that have evaporated since the beginning of the simulation) at the end of the LES at t^*=30, and the CPU time required. Comparing simulations with $N_R = 1$, the SSC LES has more drops than the GRD LES while the SMD has fewer drops at t^*=30; the CPU times are comparable. Using higher values of N_R with the GRD model leads to values of N_d at $t^* = 30$ lower than for N_R=1: by 1% for $N_R = 8$, by 4% for $N_R = 16$ and $N_R = 32$ and by 23% for $N_R = 64$. The indication for $N_R = 64$ is that an incorrect number of physical drops is being simulated, and therefore this N_R value is excessive. The reduction in N_{cd} has little impact on the CPU time beyond the 10% reduction of $N_R = 8$ compared to $N_R = 1$. This suggests that most of the computational effort is being expended on the gas phase.

3.2.1 Evolution of global quantities

Figure 7 illustrates the time evolution of various global quantities for the LES with $N_R = 1$. Initially, the domain is devoid of drops. The time evolution of N_d (Fig. 7(a)) encompasses in its history both the number of drops that have exited the domain at the outlet boundaries and the number of drops that have been removed by evaporation. By the time t^* =30, N_d oscillates around a value of 620000. Compared to the unforced jet, the forced jet requires a longer time for $N_{d,evap}$ to achieve a constant rate (Fig. 7(b)): this rate becomes constant at t^*=15 for the unforced jet but at t^*=23 for the forced jet. The longer time required for the forced jet to achieve a stationary state can be explained by the longer time required for the jet to establish its response to the inlet conditions.

The other global quantities illustrated in Fig. 7 are $\sqrt{\langle\langle\omega_1\rangle\rangle}$, $\sqrt{\langle\langle\omega_3\rangle\rangle}$, $\langle\langle\omega_i\omega_i\rangle\rangle$ (which measures stretching and tilting, an important mechanism for turbulence production), the resolved kinetic energy ($E_{kG} = \int_{\text{domain}} \rho\,(u_i u_i/2)\,dV$), $\{\{T_d\}\}$ (drop temperature) and $\{\{d^2\}\}$ (drop diameter-squared), where $\langle\langle\rangle\rangle$ denotes volumetric-averaging over the domain and $\{\{\}\}$ denotes ensemble-averaging over all the computational drops. All the global gas-phase quantities exhibit a response to the forcing, matching exactly its frequency; the drops statistics also have the same response. The GRD and SSC LES show higher levels of vorticity than the SMD LES in both the streamwise and spanwise directions; this difference is more noticeable in the streamwise direction as SMD reaches values 24% lower than the GRD LES, which in turn reaches values 14% lower than the SSC LES. Similarly, the SMD LES kinetic energy is lower, by about 5%, than that of the SSC and GRD LES (Fig. 7(f)), indicating the more dissipative nature of the SMD model. For these simulations, only a small fraction (between 0.3% and 0.4%) of the total energy in the system (E_0) is expressed as kinetic energy. For the drop statistics, $\{\{T_d\}\}$ and $\{\{d^2\}\}$ are close for all three LES models, with the SMD LES $\{\{T_d\}\}$ slightly lower (about 1%) than that of the SSC and GRD LES, and its $\{\{d^2\}\}$ being slightly higher (about 3%). The curves plotted in Fig. 7(h) do not follow the d^2 law of linear decay

as $\{\{d^2\}\}$ is an ensemble average result. Compared to the unforced jet, the forced jet has higher vorticity and enstrophy levels, created by the oscillation of the jet streamwise velocity component, and smaller hotter drops.

To determine the behavior of the dynamic models, the time evolution of the dynamic coefficients is presented in Fig. 8 for the SMD and GRD models. The SMD C_ς is not shown as its range is two to three orders of magnitude larger than that of C_τ and C_η. The distinctive feature of the time-evolution is that, for both models, the coefficients exhibit a response to the forcing, clearly seen as a pattern of repeating peaks. For example the initial perturbation has a frequency $f_0 = 1310$ Hz, almost identical to the frequency of 1308 Hz of the biggest peaks. For the GRD model, by t^*=30, the three dynamic coefficients oscillate around values (0.15 for C_τ and 0.13 for C_ς and C_η) very close to the values calibrated on the DNS database of the temporal mixing layer configuration[7] (of 0.15), suggesting the universality of GRD SGS-modeling in different flow configurations.

3.2.2 Flow visualizations

Complementing the global quantities, flow visualizations allow for a qualitative comparison of the different SGS models. Plotted in Fig. 9 are ω_3 and $\omega_i\omega_i$ for the GRD, SMD and SSC LES with $N_R = 1$ at $t^* = 30$, in the spanwise center-plane ($x_3 = 0$). For each case, five vortices are present. The three models have similar predictions of the size and location of each vortex, although the SMD has slightly higher local magnitude of vorticity. These findings are consistent to those for the temporal mixing layer,[20] where the SMD model only captured the largest scale vortices but was unable to reproduce smaller structures, as the jet here shows little small-scale activity. Figure 10 shows ω_3 at three different downstream locations, and the vortices of Fig. 9 are seen to be symmetrical to the plane $x_3 = 0$. The vortices in the three LES have similar shapes and vorticity levels as they are convected downstream.

Plotted in Fig. 11 are ρ_n and Y_V, at the same time and in the same plane as in Fig. 9. As for the vorticity, all LES have similar results, although the SMD LES has slightly higher ρ_n and Y_V. The LES show regions of low ρ_n, which correspond to regions of high vorticity in Fig. 9, consistent with experimental findings.[31] Figure 12 shows ρ_n at the same planes as Fig. 10, and here again the three LES resemble one another, although the SMD LES ρ_n at the farthest downstream location seems slightly less uniform that the GRD and SSC LES at the same location.

Finally, to assess the performance of the computational-drop modeling as N_{cd} is reduced, Fig. 13 shows ρ_n and Y_V using the GRD model for increasing values of N_R from 8 to 64; the $N_R = 1$ results are plotted in Fig. 11. Up to a reduction of 32, both ρ_n and Y_V are still well predicted by the GRD model, although some denser region of drops appear at $N_R = 32$. The $N_R = 64$ LES exhibit degradation of the distribution of ρ_n, although qualitatively it still matches the lower N_R results and has similar ρ_n levels as $N_R = 32$. The vapor mass fraction, however, is still well predicted for $N_R = 64$ compared to $N_R = 1$. The indications from Table 1 that $N_R = 32$ is the maximal accurate drop reduction are therefore confirmed; this value was also obtained in the mixing layer LES.[20]

4 Conclusions

LES of a jet laden with evaporating drops were conducted using various SGS-flux models: dynamic Smagorinsky (SMD), dynamic Gradient (GRD) and constant-coefficient Scale-Similarity (SSC). The SSC model used a coefficient previously calibrated on a DNS database, while the dynamic models did not require calibration as their model coefficients were computed from the LES field during LES. An accurate numerical algorithm, sixth-order in space and fourth-order in time, was used to integrate the gas-phase and drop evolution equations. The drops were tracked in a Lagrangian frame, while the gas-phase was computed in an Eulerian frame. The effect of (physical or computational) drops on the flow field was embodied in filtered source terms (FSTs) in the gas-phase equations, and the drops were taken to be affected by the filtered flow field, without direct SGS effects. The SGS models were essential to LES, as the absence of any SGS models caused the simulations to end after only a few time steps. LES of an unforced jet with a jet-diameter Reynolds number of 500, using the GRD model and the same number of computational as physical drops, were compared to previous DNS of similar flow conditions. The steady-state was reached at the same time for LES as the DNS, and LES-predicted vorticity and streamwise mass flux were in good agreement with the DNS.

LES of a forced jet was conducted for the same jet Reynolds number as for the unforced jet, using the same number of computational as physical drops. Similar results were obtained from the three SGS models, both for global and local quantities, including vorticity components, drop number density and vapor mass fraction. The LES all showed regions of low drop number density corresponding to high vorticity regions. However, no small scale structures were observed; this lack of small structure contributed to the similar performance of the three SGS models, as the SMD model has previously been shown to perform poorly in replicating the resolved small scales. Using the GRD model, the number of computational drops was reduced, with up to a factor of 64 fewer computational than physical drops. The LES with a reduction factor of 32 retained most of the characteris-

tics of the LES with the full number of physical drops, but degradation of the results was observed for a reduction factor of 64. Future studies should involve higher values of the jet Reynolds number, and perhaps different inflow conditions, in order to generate fully turbulent flow which will place more demands on the LES models.

Acknowledgements

This work was conducted at the Jet Propulsion Laboratory (JPL) of the California Institute of Technology (Caltech) under the sponsorship of the U.S. Department of Energy, with R. Danz and D. Hooker serving as contract monitors, under an agreement with the National Aeronautics and Space Administration. Computations were performed on the SGI Origin 2000 at the JPL Supercomputing Center.

References

[1]Boivin, M., Simonin, O., and Squires, K., "Direct Numerical Simulation of Turbulence Modulation by Particles in Isotropic Turbulence," *Journal of Fluid Mechanics*, Vol. 375, 1998, pp. 235–263.

[2]Mashayek, F. and Jaberi, F., "Particle Dispersion in Forced Isotropic Low-Mach-Number Turbulence," *International Journal of Heat and Mass Transfer*, Vol. 42, 1999, pp. 2823–2836.

[3]Mashayek, F., "Direct Numerical Simulations of Evaporating Droplet Dispersion in Forced Low-Mach-Number Turbulence," *International Journal of Heat and Mass Transfer*, Vol. 41, No. 17, 1998, pp. 2601–2617.

[4]Réveillon, J. and Vervisch, L., "Spray Vaporization in Nonpremixed Turbulent Combustion Modeling: A Single Drop Model," *Combustion and Flame*, Vol. 121, 2000, pp. 75–90.

[5]Miller, R. and Bellan, J., "Direct Numerical Simulation of a Confined Three-Dimensional Gas Mixing Layer with One Evaporating Hydrocarbon-Droplet Laden Stream," *Journal of Fluid Mechanics*, Vol. 384, 1999, pp. 293–338.

[6]Miller, R. and Bellan, J., "Direct Numerical Simulation and Subgrid Analysis of a Transitional Droplet Laden Mixing Layer," *Physics of Fluids*, Vol. 12, No. 3, March 2000, pp. 650–671.

[7]Okong'o, N. and Bellan, J., "Consistent Large Eddy Simulation of a Temporal Mixing Layer Laden with Evaporating Drops. Part 1: Direct Numerical Simulation, Formulation and *A Priori* Analysis," *Journal of Fluid Mechanics*, Vol. 499, 2004, pp. 1–47.

[8]Abdel-Hameed, H. and Bellan, J., "Direct Numerical Simulations of Two-Phase Laminar Jet Flows with Different Cross-Section Injection Geometries," *Physics of Fluids*, Vol. 14, No. 10, October 2002, pp. 3655–3674.

[9]Boivin, M., Simonin, O., and Squires, K., "On the Prediction of Gas-Solid Flows with Two-Way Coupling Using Large Eddy Simulation," *Physics of Fluids*, Vol. 12, No. 8, 2000, pp. 2080–2090.

[10]Deutsch, E. and Simonin, O., "Large Eddy Simulation Applied to the Modelling of Particulate Transport Coefficients in Turbulent Two-Phase Flows," *Eighth Symposium on Turbulent Shear Flows*, September 1991, pp. 10–1:1–6.

[11]Simonin, O., Deutsch, E., and Boivin, M., "Large Eddy Simulation and Second-Moment Closure of Particle Fluctuating Motion in Two-Phase Turbulent Shear Flows," *Turbulent Shear Flows*, Vol. 9, 1993, pp. 85–115.

[12]Uijttewaal, W. and Oliemans, R., "Particle Dispersion and Deposition in Direct Numerical and Large Eddy Simulations of Vertical Pipe Flows," *Physics of Fluids*, Vol. 8, No. 10, 1996, pp. 2590–2604.

[13]Wang, Q. and Squires, K., "Large Eddy Simulations of Particle-Laden Turbulent Channel Flow," *Physics of Fluids*, Vol. 8, No. 5, 1996, pp. 1207–1223.

[14]Yamamoto, Y., Potthoff, M., Tanaka, T., Kajishima, T., and Tsuji, Y., "Large-Eddy Simulation of Turbulent Gas-Particle Flow in a Vertical Channel: Effect of Considering Inter-Particle Collisions," *Journal of Fluid Mechanics*, Vol. 442, 2001, pp. 303–334.

[15]Smagorinksy, J., "Some Historical Remarks on the Use of Nonlinear Viscosities," *Large Eddy Simulation of Complex Engineering and Geophysical Flows*, edited by B. Galperin and S. Orszag, chap. 1, Cambridge University Press, 1993, pp. 3–36.

[16]Glaze, D. and Frankel, S., "Effect of Dispersion Characteristics on Particle Temperature in an Idealized Nonpremixed Reacting Jet," *International Journal of Multiphase Flow*, Vol. 26, 2000, pp. 609–633.

[17]Kurose, R. and Makino, H., "Large Eddy Simulation of a Solid-Fuel Jet Flame," *Combustion and Flame*, Vol. 135, 2003, pp. 1–16.

[18]Apte, S., Mahesh, K., Moin, P., and Oefelein, J., "Large-Eddy Simulation of Swirling Partcle-Laden Flows in a Coaxial-Jet Combustor," *International Journal of Multiphase Flow*, Vol. 29, 2003, pp. 1311–1331.

[19]Nadaoka, K., Nihei, Y., and Yagi, H., "Grid-Averaged Lagrangian LES Model for Multiphase Turbulent Flow," *International Journal of Multiphase Flow*, Vol. 25, 1999, pp. 1619–1643.

[20]Leboissetier, A., Okong'o, N., and Bellan, J., "Consistent Large Eddy Simulation of a Temporal Mixing Layer Laden with Evaporating Drops. Part 2: *A Posteriori* Analysis," 2004, To be submitted.

[21]Bardina, J., Ferziger, J., and Reynolds, W., "Improved Subgrid Scale Models for Large Eddy Simulation," Tech. Rep. 80-1357, AIAA, 1980.

[22]Crowe, C., Chung, J., and Troutt, T., "Particle Mixing in Free Shear Flows," *Progress in Energy and Combustion Science*, Vol. 14, 1998, pp. 171–194.

[23]Yoshizawa, A., "Statistical Theory for Compressible Turbulent Shear Flows, With the Application to Subgrid Modeling," *Physics of Fluids*, Vol. 29, No. 7, 1986, pp. 2152–2164.

[24]Clark, R., Ferziger, J., and Reynolds, W., "Evaluation of Subgrid-Scale Models Using an Accurately Simulated Turbulent Flow," *Journal of Fluid Mechanics*, Vol. 91, No. 1, 1979, pp. 1–16.

[25]Germano, M., Piomelli, U., Moin, P., and Cabot, W., "A Dynamic Subgrid-Scale Eddy Viscosity Model," *Physics of Fluids A*, Vol. 3, No. 7, 1991, pp. 1760–1765.

[26]Lilly, D., "A Proposed Modification of the Germano Subgrid-Scale Closure Method," *Physics of Fluids A*, Vol. 4, No. 3, March 1992, pp. 633–635.

[27]Vreman, B., Geurts, B., and Kuerten, H., "Large-Eddy Simulation of the Turbulent Mixing Layer," *Journal of Fluid Mechanics*, Vol. 339, 1997, pp. 357–390.

[28]Poinsot, T. and Lele, S., "Boundary Conditions for Direct Simulations of Compressible Viscous Flows," *Journal of Computational Physics*, Vol. 101, 1992, pp. 104–129.

[29]Kennedy, C. and Carpenter, M., "Several New Numerical Methods for Compressible Shear Layer Simulations," *Applied Numerical Mathematics*, Vol. 14, 1994, pp. 397–433.

[30]Liepmann, D. and Gharib, M., "The Role of Streamwise Vorticity in the Near-Field Entrainment of Round Jets," *Journal of Fluid Mechanics*, Vol. 245, 1992, pp. 643–668.

[31]Squires, K. and Eaton, J., "Preferential Concentration of Particles by Turbulence," *Physics of Fluids A*, Vol. 3, No. 5, 1991, pp. 1169–1178.

SGS Model	N_R	$t^* = 30$		
		N_d	$N_{d,evap}$	CPU-hours
GRD	1	626 414	23 405	265
GRD	8	619 648	24 416	242
GRD	16	598 592	25 632	240
GRD	32	601 184	24 768	239
GRD	64	480 896	43 072	240
SMD	1	609 343	15 434	288
SSC	1	647 212	31 990	259

Dimensionless time, $t^* = t\Delta U_0/D_J$
$N_{d,evap}$ is the cumulative number of physical drops that have evaporated during of the simulation.
CPU hours on 32 processors of an SGI Origin2000.

Table 1 Summary of LES runs; forced jet.

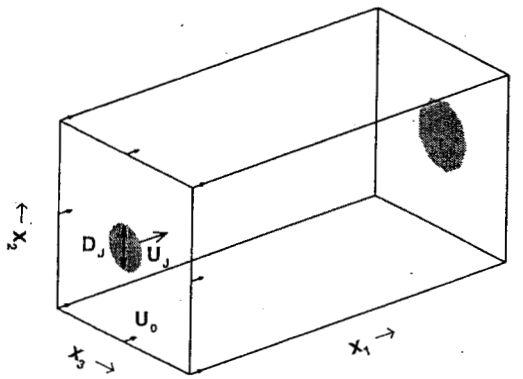

Fig. 1 Circular jet configuration: inlet plane at $x_1 = 0$, drops injected through circular orifice of diameter D_J centered at $x_2 = 0, x_3 = 0$.

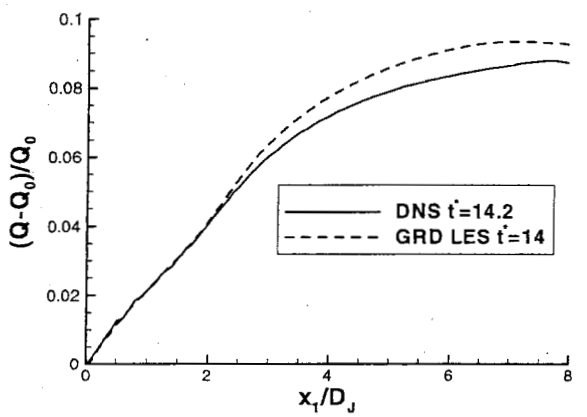

Fig. 2 Steady state streamwise mass flux for unforced jet: DNS and LES.

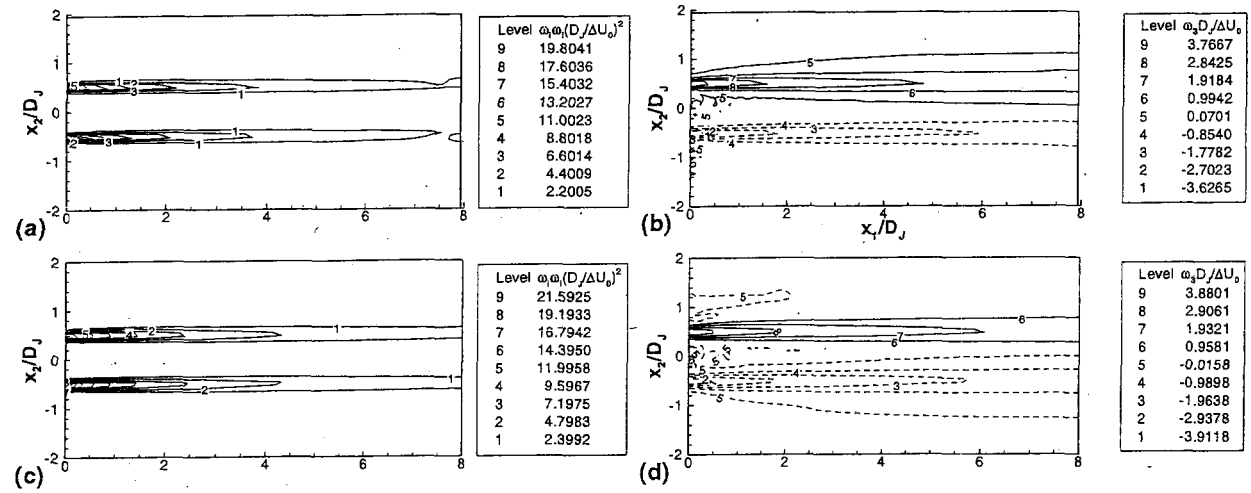

Fig. 3 Unforced jet at t^*=14 and x_3/D_J=0, DNS (top) and LES using GRD model and N_R=1 (bottom): (a,c) vorticity magnitude, (b,d) spanwise vorticity. Dashed lines are used for negative values.

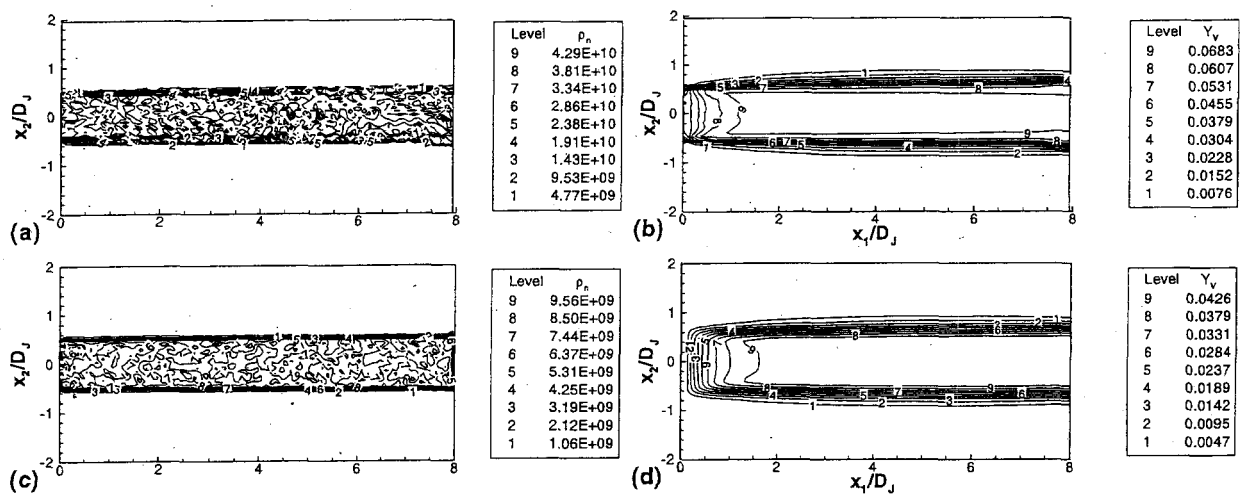

Fig. 4 Unforced jet at t^*=14 and x_3/D_J=0, DNS (top) and LES using GRD model and N_R=1 (bottom): (a,c) drop number density (m^{-3}) and (b,d) vapor mass fraction.

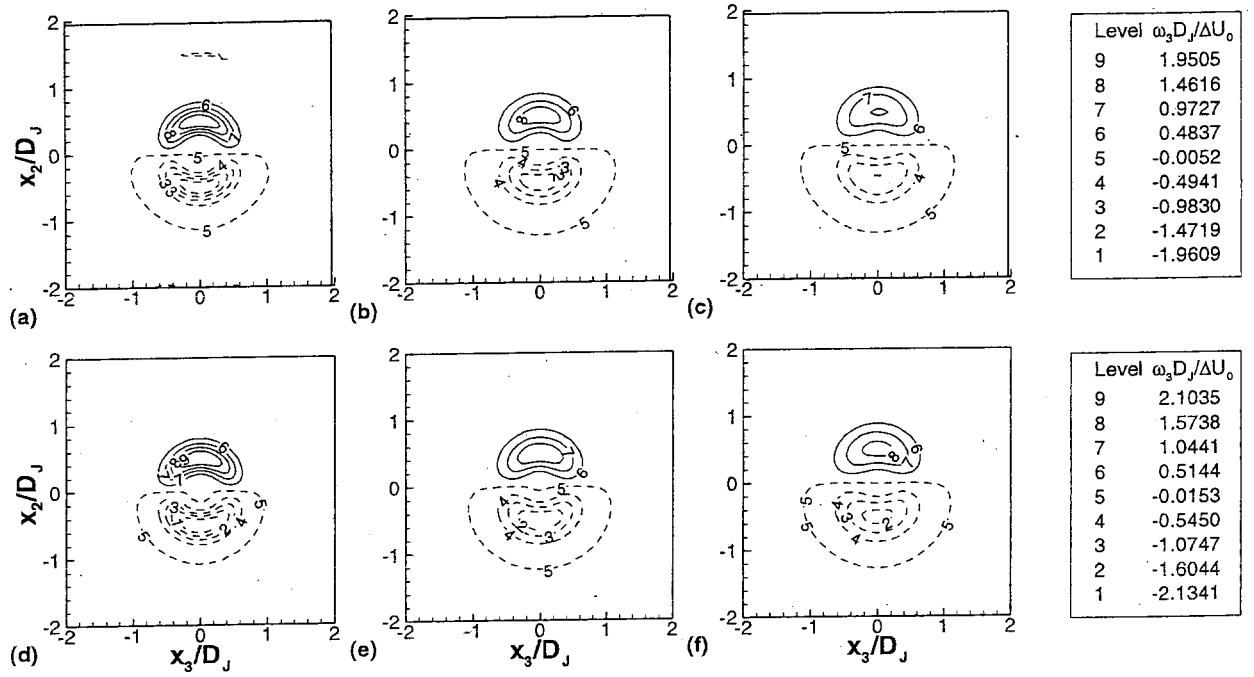

Fig. 5 Spanwise vorticity, unforced jet at t^*=14: DNS (top) and LES using GRD model and N_R=1 (bottom) at x_1/D_J=2.5 (a,d); 5.0 (b,e); 7.5 (c,f). Dashed lines are used for negative values.

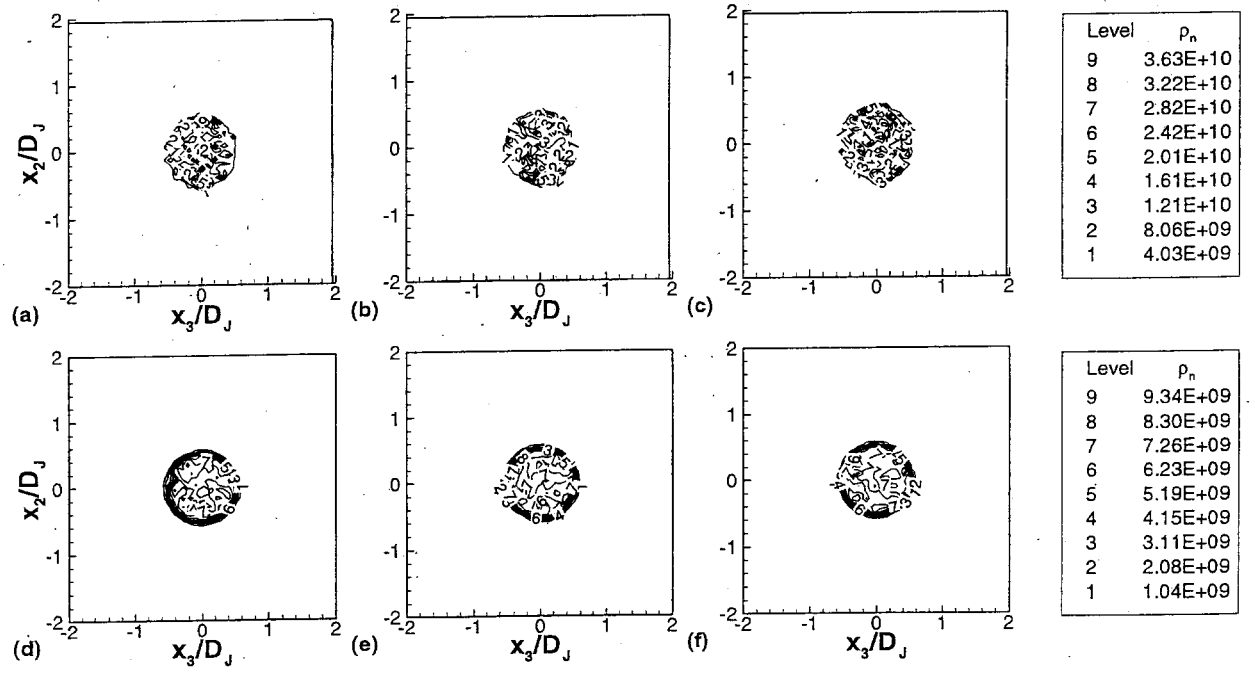

Fig. 6 Drop number density (m^{-3}), unforced jet at t^*=14: DNS (top) and LES using GRD model and N_R=1 (bottom) at x_1/D_J=2.5 (a,d); 5.0 (b,e); 7.5 (c,f).

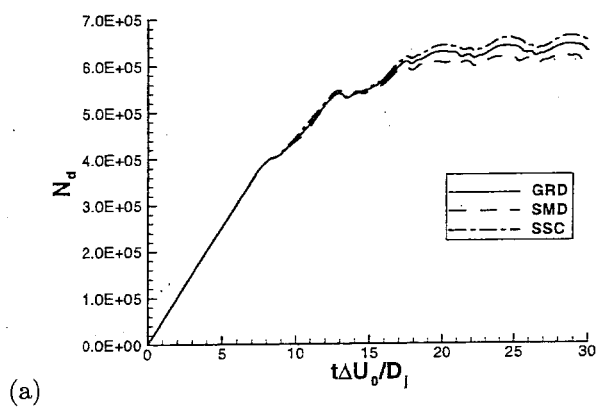

(a)

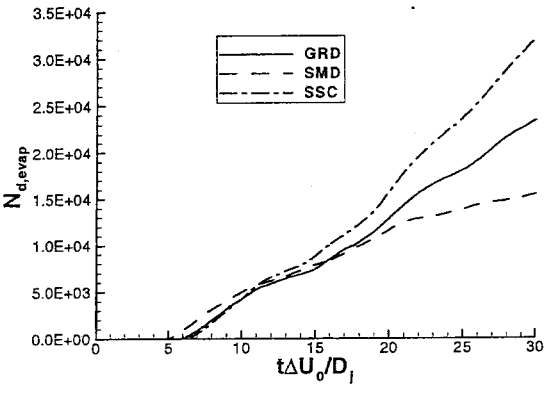

(b)

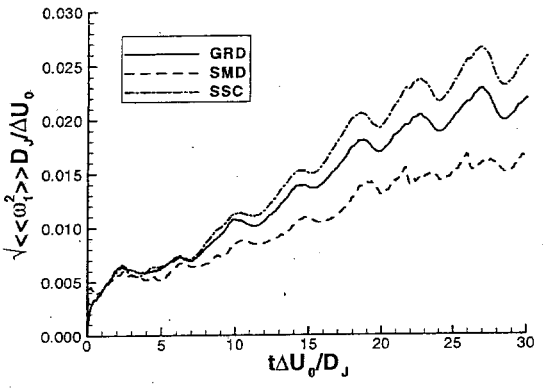

(c)

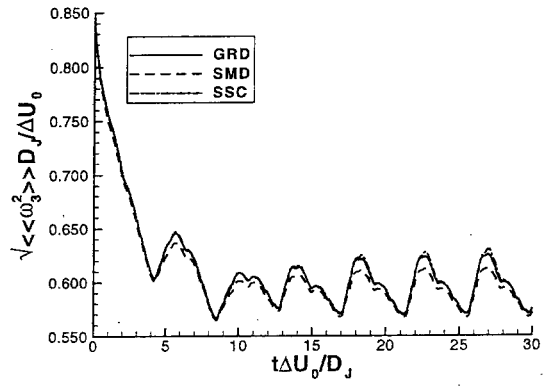

(d)

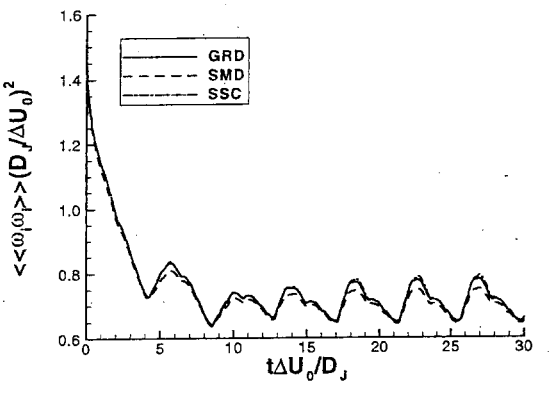

(e)

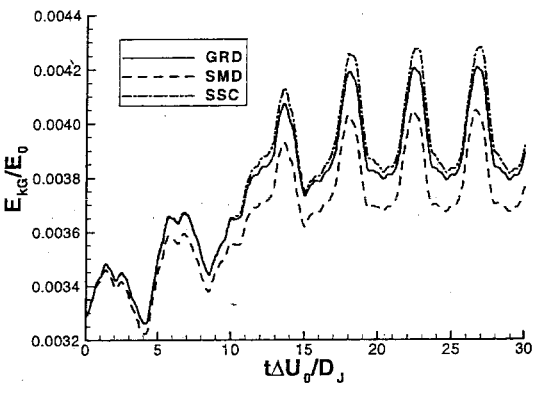

(f)

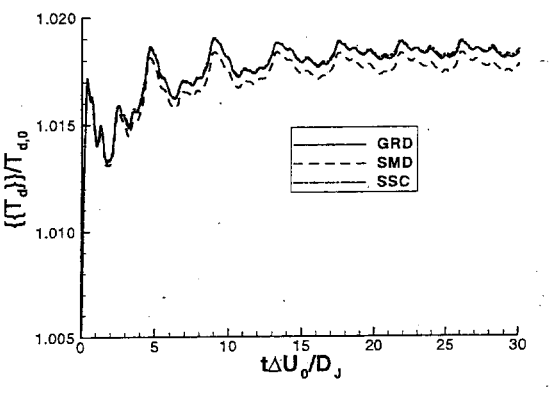

(f)

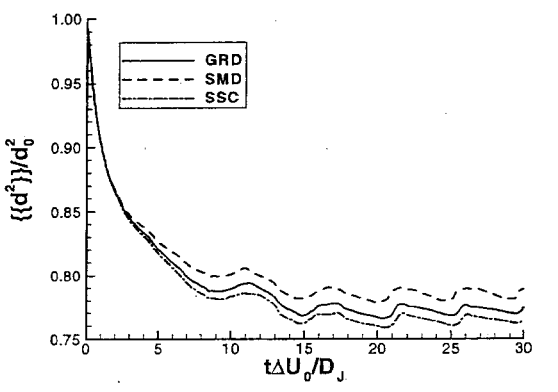

(g)

Fig. 7 Time evolution of global quantities for LES using $N_R = 1$ and the SMD, GRD and SSC SGS-flux models: (a) number of drops in domain, (b) cumulative number of evaporated drops, (c) spanwise vorticity, (d) streamwise vorticity, (e) enstrophy, (f) resolved kinetic energy, (g) drop temperature and (h) drop diameter-squared.

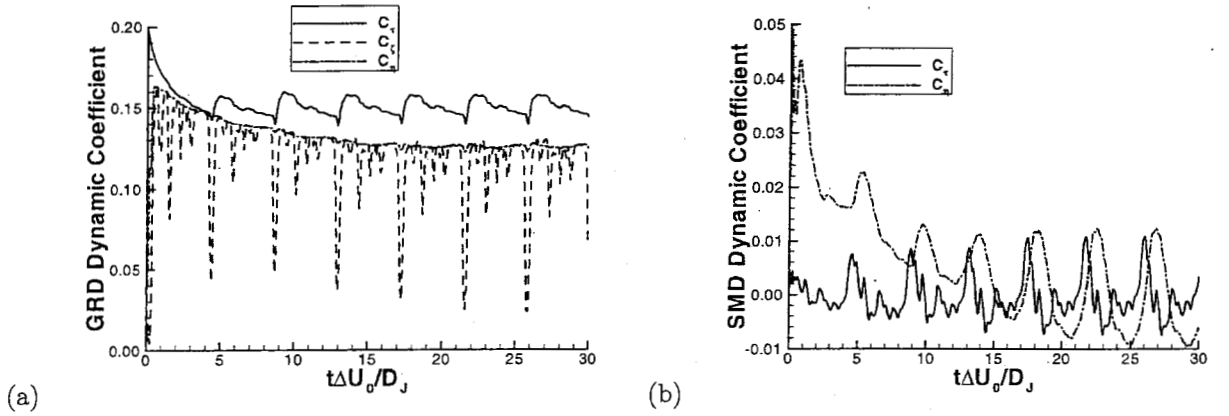

Fig. 8 Time evolution of the dynamic coefficients: (a) GRD LES and (b) SMD LES; N_R=1.

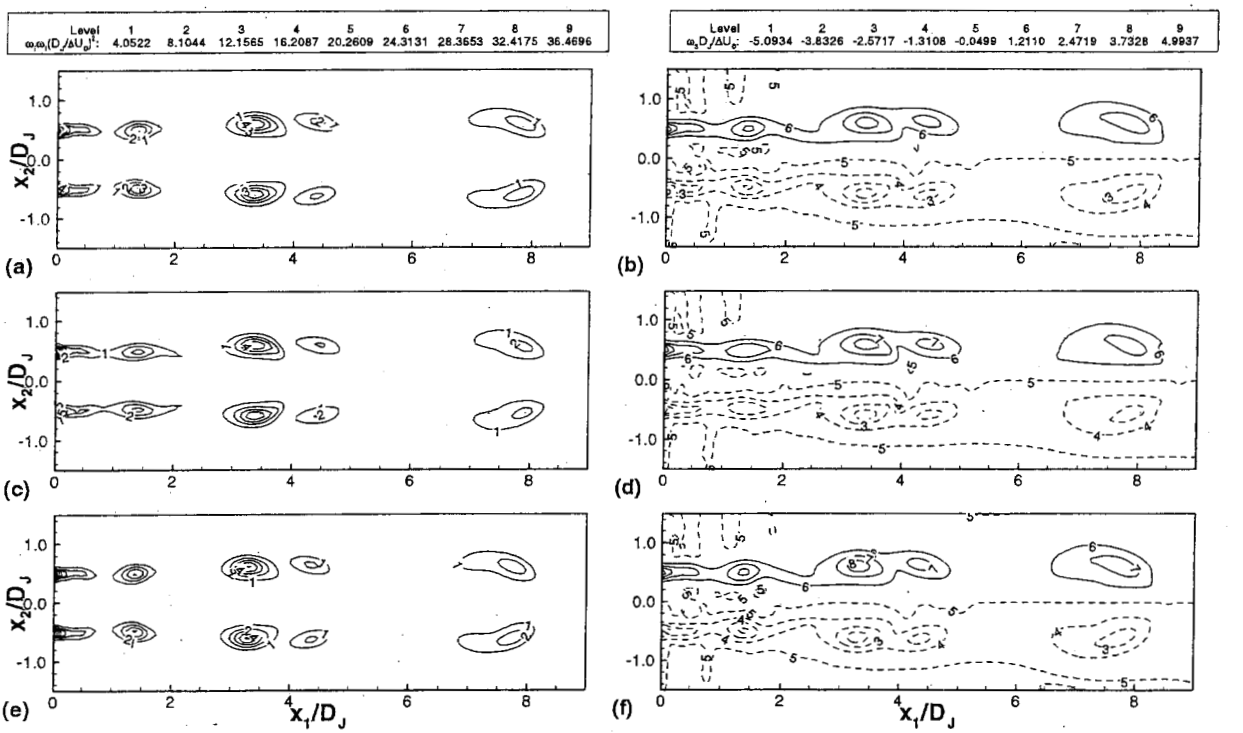

Fig. 9 Vorticity magnitude (a,c,e) and spanwise vorticity (b,d,f) at $t^* = 30$ and $x_3/D_J = 0$: (a,b) GRD LES, (c,d) SMD LES and (e,f) SSC LES; N_R=1. Dashed lines are used for negative values.

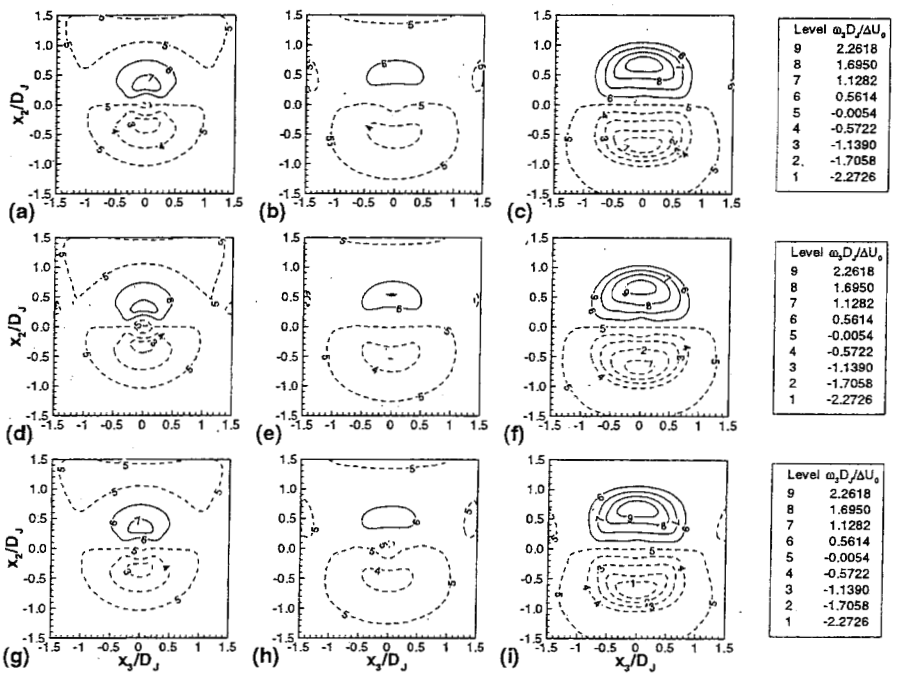

Fig. 10 Spanwise vorticity for (a,b,c) GRD LES, (d,e,f) SMD LES and (g,h,i) SSC LES at $t^* = 30$ and x_1/D_J=2.5 (a,d,g); 5.0 (b,e,h); 7.5 (c,f,i); N_R=1.

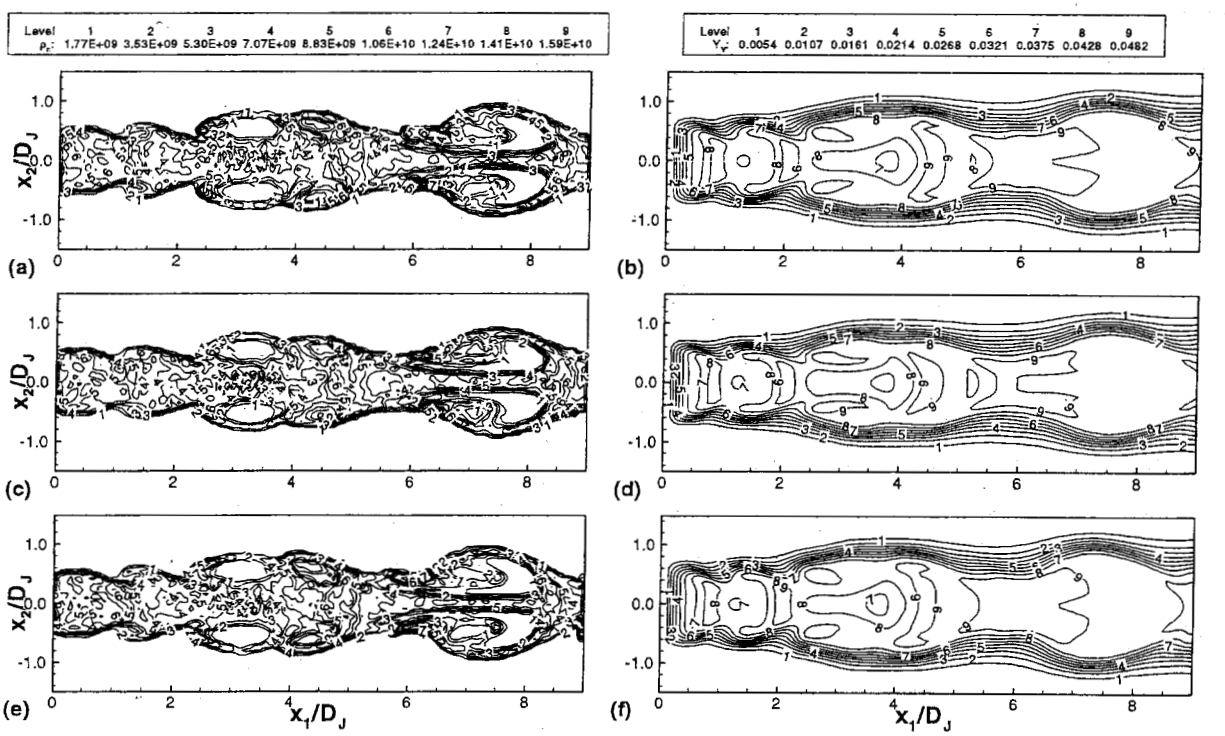

Fig. 11 Drop number density (m^{-3}) (a,c,e) and vapor mass fraction (b,d,f) at $t^* = 30$, and $x_3/D_J = 0$: (a,b) GRD LES, (c,d) SMD LES and (e,f) SSC LES; N_R=1.

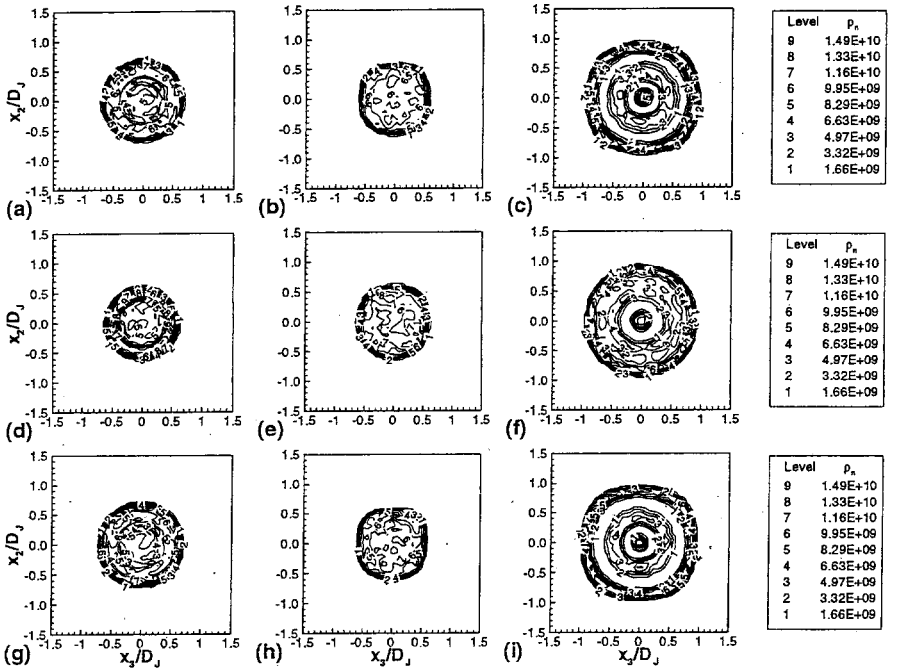

Fig. 12 Drop number density (m−3) for (a,b,c) GRD LES, (d,e,f) SMD LES and (g,h,i) SSC LES at $t^* = 30$ and x_1/D_J=2.5 (a,d,g); 5.0 (b,e,h); 7.5 (c,f,i); N_R=1.

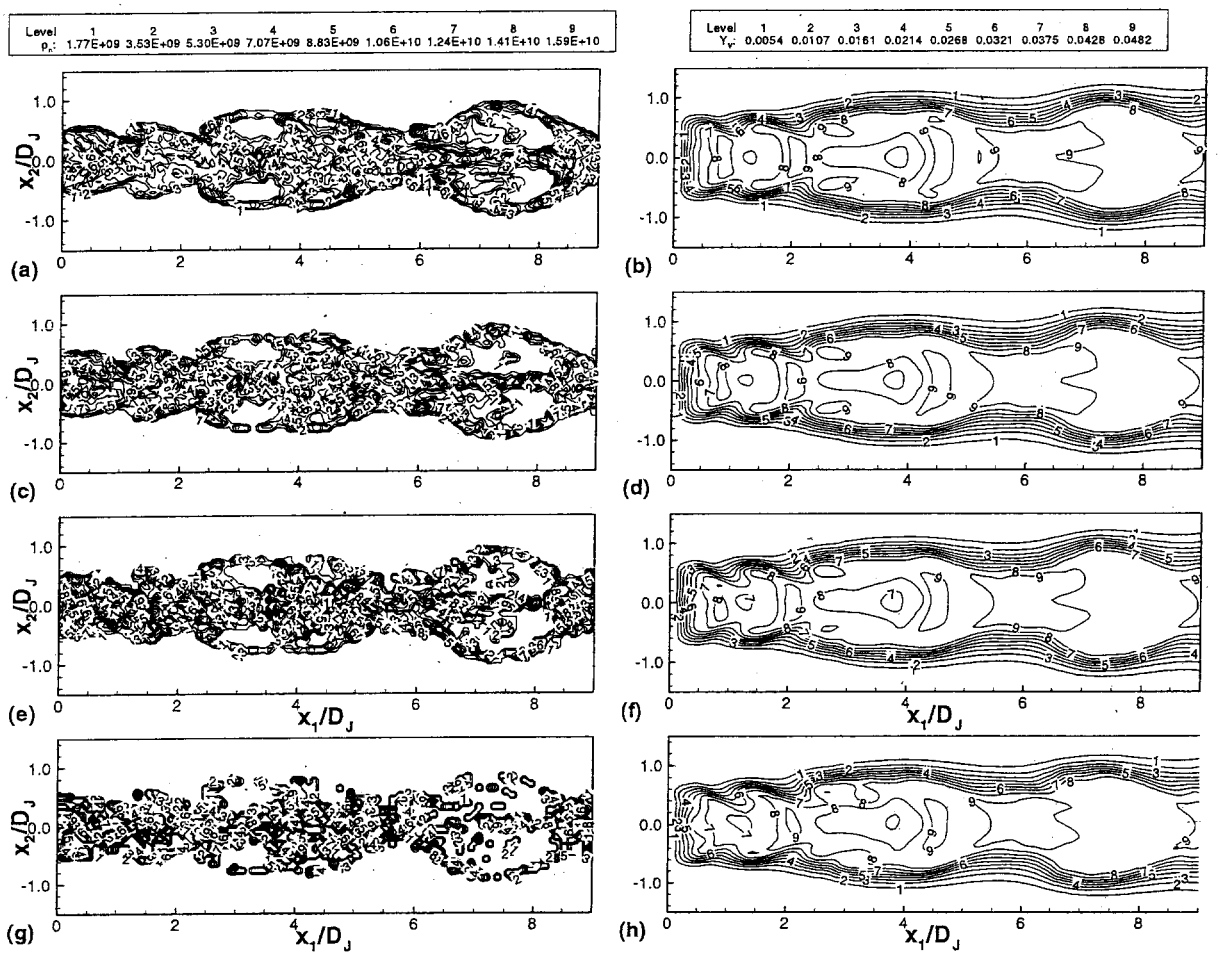

Fig. 13 Drop number density (m^{-3}) (a,c,e,g) and vapor mass fraction (b,d,f,h), at t^*=30 and x_3/D_J=0, for GRD LES: (a,b) $N_R = 8$, (c,d) $N_R = 16$, (e,f) $N_R = 32$ and (g,h) $N_R = 64$.